Sensors & Diagnostics

PAPER

View Article Online
View Journal | View Issue



Cite this: *Sens. Diagn.*, 2025, **4**, 803

# Ultrasensitive electrochemical detection of methotrexate in biological fluids using $NiMn_2O_4$/CNT nanocomposite-modified electrode†

Nasir Abbas and Tae Hyun Kim *

Received 9th May 2025,
Accepted 10th July 2025

DOI: 10.1039/d5sd00064e

rsc.li/sensors

Methotrexate (MTX) is a widely used chemotherapeutic drug with a narrow therapeutic index, making its precise monitoring crucial for effective treatment and minimizing side effects. This study focuses on the development of a clinically applicable $NiMn_2O_4$/CNT nanocomposite-modified glassy carbon electrode ($NiMn_2O_4$/CNT-GCE) for the sensitive and selective electrochemical detection of MTX. The $NiMn_2O_4$ nanomaterial was synthesized *via* a co-precipitation method followed by calcination, and its composite with CNTs was optimized to enhance electrochemical performance. The sensor demonstrated a detection limit as low as 0.627 nM and a broad linear detection range (0.05–3 μM), attributed to the synergistic effects of $NiMn_2O_4$ and CNTs that enhance electron transfer and active site availability. Moreover, the $NiMn_2O_4$/CNT-GCE was successfully applied to detect MTX in spiked serum and urine samples, achieving recovery rates of 96–99% with relative standard deviations below 3.5%. Its minimal interference with common metabolites and excellent stability makes it ideal for therapeutic drug monitoring. This work underscores the potential of $NiMn_2O_4$/CNT as a promising platform for real-time clinical diagnostics and advanced electrochemical sensing applications.

## 1. Introduction

Methotrexate (MTX) is a widely used chemotherapeutic and immunosuppressive drug, extensively employed in the treatment of cancers such as leukemia[1] and autoimmune diseases,[2] including rheumatoid arthritis.[3–5] Despite its therapeutic benefits, MTX poses significant risks due to its narrow therapeutic index.[6] Excessive dosages can lead to severe toxic side effects,[7] including hepatotoxicity and bone marrow suppression, while sub-therapeutic levels may result in reduced efficacy.[8,9] Consequently, precise and reliable monitoring of MTX levels in biological fluids is essential to ensure patient safety and optimize therapeutic outcomes.[10–13]

Conventional techniques for MTX detection, such as high-performance liquid chromatography (HPLC),[14,15] enzyme-linked immunosorbent assays (ELISA),[16,17] and mass spectrometry,[18] are well-established for their sensitivity and specificity.[18] However, these methods are often associated with limitations, including high operational costs, labor-intensive sample preparation, and the requirement for sophisticated instrumentation.[19–21] Given these challenges, electrochemical sensors offer a compelling alternative due to their simplicity, rapid response times, and exceptional sensitivity, making them ideal for real-time drug monitoring.[22–25]

The performance of electrochemical sensors heavily depends on the electrode material, which plays a pivotal role in enhancing electrocatalytic activity and stability.[26,27] Nickel manganese oxide ($NiMn_2O_4$), a spinel-type oxide, has garnered significant attention in electrochemical applications due to its unique properties, including high electrical conductivity, multiple redox states, and synergistic interactions between nickel and manganese ions.[28–32] Despite these advantages, standalone $NiMn_2O_4$ often suffers from moderate conductivity and limited surface area, which can hinder its practical application.

To address these limitations, $NiMn_2O_4$ can be combined with carbon nanotubes (CNTs), which serve as an excellent supporting matrix due to their remarkable electrical conductivity, high surface area, and mechanical stability.[33,34] The integration of $NiMn_2O_4$ and CNTs into a composite material leverages the complementary properties of both components, providing a synergistic effect that enhances electron transfer, increases active sites, and improves overall sensor performance.[35]

In this study, we employed a two-step approach to develop a highly sensitive electrochemical sensor for MTX detection (Scheme 1). In the first step, a $NiMn_2O_4$/CNT nanocomposite

*Department of Chemistry, Soonchunhyang University, Asan, 31538, Republic of Korea. E-mail: thkim@sch.ac.kr*

† Electronic supplementary information (ESI) available: Supplementary data associated with this article can be found in the online version. See DOI: https://doi.org/10.1039/d5sd00064e

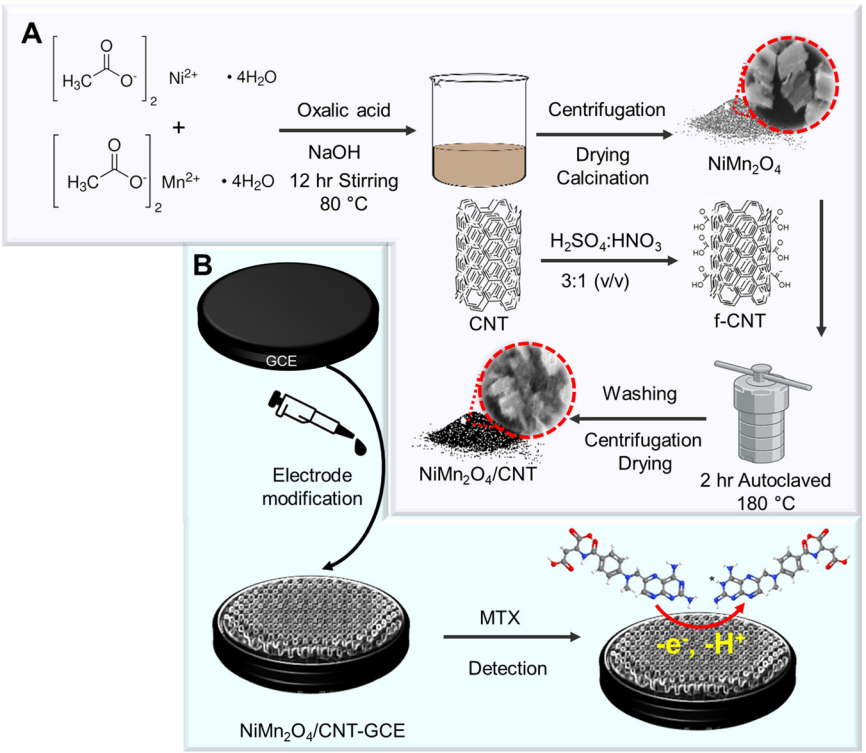


**Scheme 1** (A) Schematic representation of the two-step synthesis process for the $NiMn_2O_4$/CNT composite: co-precipitation of $NiMn_2O_4$ followed by hydrothermal treatment with functionalized CNTs. (B) Fabrication of the $NiMn_2O_4$/CNT-modified glassy carbon electrode ($NiMn_2O_4$/CNT-GCE) and its application for the electrochemical detection of methotrexate (MTX).

was synthesized using a co-precipitation method followed by calcination[36] and hydrothermal treatment with functionalized CNTs to optimize the composite's electrochemical properties.[37,38] In the second step, the nanocomposite was use d to fabricate a modified glassy carbon electrode ($NiMn_2O_4$/CNT-GCE), which was applied for the electrochemical detection of MTX. This systematic workflow ensured the enhancement of both material properties and sensor performance.

The $NiMn_2O_4$/CNT composite and its modified electrode were systematically characterized using X-ray diffraction (XRD), scanning electron microscopy (SEM), and transmission electron microscopy (TEM), while the electrochemical performance was evaluated using cyclic voltammetry (CV) and differential pulse voltammetry (DPV). The sensor demonstrated remarkable sensitivity and selectivity, achieving a detection limit as low as 0.627 nM and a wide linear range of 0.05–3 μM.

The practical applicability of the sensor was validated through the detection of MTX in spiked serum and urine samples, achieving recovery rates of 96–99% with relative standard deviations below 3.5%. These results highlight its potential for clinical diagnostics. To the best of our knowledge, this study represents the first application of a $NiMn_2O_4$/CNT composite for MTX detection, offering a novel contribution to the field of electrochemical sensing and paving the way for real-time therapeutic drug monitoring.

## 2. Experimental

### 2.1. Chemicals

The materials and reagents used in this synthesis were of analytical grade and sourced from Sigma Aldrich. All chemicals were employed directly without further purification. The following were utilized: nickel(II) acetate tetrahydrate ($Ni(CH_3COO)_2{\cdot}4H_2O$, 99.99% purity), oxalic acid ($C_2H_2O_4$), manganese(II) acetate tetrahydrate ($Mn(CH_3COO)_2{\cdot}4H_2O$, 99.99% purity), sodium hydroxide (NaOH), and ethanol ($C_2H_5OH$, 99.08% purity). Human serum was purchased from Sigma-Aldrich and used as received. Human urine samples were voluntarily provided by a healthy adult donor from the research group with informed consent. The samples were anonymized and used solely for research purposes in accordance with institutional ethical guidelines. Given the non-invasive nature of the sample collection and lack of identifying information, IRB approval was not required. A phosphate buffer solution (0.05 M PBS) was prepared by dissolving the appropriate amounts of disodium hydrogen phosphate ($Na_2HPO_4$) and monosodium hydrogen phosphate ($NaH_2PO_4$) in deionized (DI) water. For electrode preparation, carbon black was used. Commercially purchased multi-walled carbon nanotubes (CNTs) with a diameter of 1–2 nm and a length of approximately 50 μm were also included. Deionized water was used as the solvent throughout the study.

### 2.2. Instrumentation

To thoroughly understand the structure and properties of the synthesized catalysts, a variety of characterization techniques were employed. XRD analysis, performed using a Rigaku MiniFlex600 (Japan), provided insight into the crystal structure of the materials. XPS, conducted with a K-Alpha (Thermo Fisher Scientific, USA), verified the chemical composition of the $NiMn_2O_4$/CNT nanocomposite, specifically examining the binding energies of key elements such as nickel, oxygen, and carbon. SEM using a ZEISS Sigma 500 (Germany) offered an initial view of the surface morphology and microstructure. For higher-resolution imaging, field emission scanning electron microscopy (FE-SEM; TESCAN MIRA LMH, Czech Republic) was performed to provide detailed surface and structural insights. TEM (JEOL JEM-1010, Japan) offered a deeper understanding of the nanocomposite's intricate structural features.

The electrochemical properties of the materials were evaluated using a CHI 660D electrochemical workstation (CH Instruments, USA) in a standard three-electrode configuration. In this setup, a platinum wire served as the counter electrode, an Ag/AgCl electrode was used as the reference electrode, and the working electrode was either a bare GCE (diameter of 3.0 mm) or one modified with the $NiMn_2O_4$/CNT nanocomposite.

Electrochemical impedance spectroscopy (EIS) was performed to assess the interfacial charge transfer properties of the $NiMn_2O_4$/CNT-modified electrode. The measurements were conducted over a frequency range of 1 Hz to 100 kHz, with an AC amplitude of 5 mV at an open circuit potential (OCP) of 0.267 V for bare GCE, 0.247 V for CNT-GCE, 0.250 V for $NiMn_2O_4$-GCE, and 0.249 V for $NiMn_2O_4$/CNT-GCE.

### 2.3. Synthesis of $NiMn_2O_4$

$NiMn_2O_4$ was synthesized using a co-precipitation method. Initially, 100 mL of a solution containing 0.025 M nickel acetate tetrahydrate ($Ni(CH_3COO)_2{\cdot}4H_2O$) and 0.05 M manganese(II) acetate tetrahydrate ($Mn(CH_3COO)_2{\cdot}4H_2O$) was prepared by dissolving the precursors in a 1 : 1 volume ratio of DI water and ethanol. The two solutions were mixed thoroughly to obtain a clear solution. Subsequently, 5 g of oxalic acid crystals were added, and the mixture was stirred at 700 rpm for 15 minutes at room temperature to ensure homogeneity.

Next, 100 mL of 1 M NaOH was slowly added to the solution, followed by continuous stirring for 12 hours at 80 °C. Upon completion, the resulting solution was cooled to room temperature, and the precipitate was collected *via* centrifugation at 8000 rpm. The precipitate was washed several times with ethanol and water to remove impurities, then dried overnight in a vacuum oven at 60 °C. Finally, the dried material was calcined at 450 °C for 2 hours to achieve the desired crystalline phase of $NiMn_2O_4$.[36]

### 2.4. Synthesis of $NiMn_2O_4$/CNT nanocomposite

The synthesis of the $NiMn_2O_4$/CNT nanocomposite involved the acid treatment of pristine CNTs. Specifically, 0.1 g of pristine CNTs was dispersed in a mixture of nitric acid ($HNO_3$) and sulfuric acid ($H_2SO_4$) at a volume ratio of 1 : 3 in 80 mL of DI water. The resulting mixture underwent ultrasonication for 4 hours to facilitate functionalization. After this period, the mixture was cooled to room temperature. The acid-treated CNTs were thoroughly washed with DI water until a neutral pH was achieved and then dried overnight in a vacuum oven at 60 °C. This acid treatment introduces carboxyl (–COOH) groups onto the CNT surface, which enhances their dispersion in aqueous media and promotes better interfacial interaction with metal oxides. These surface modifications improve the electron transfer properties of the resulting nanocomposite, thereby contributing to the improved electrochemical performance of the $NiMn_2O_4$/CNT sensor.

For the nanocomposite synthesis, 16.6 mg of the acid-treated CNTs was added to a beaker containing 10 mL of DI water. Separately, 225 mg of the prepared $NiMn_2O_4$ was dispersed in 10 mL of DI water. This ratio ($NiMn_2O_4$ : CNT = ~13.6 : 1, w/w) was selected based on preliminary trials that showed optimal electrochemical performance in terms of current response and stability. While other ratios were briefly explored (*e.g.*, 5 : 1 and 20 : 1), the selected formulation provided the best balance between conductivity and catalytic activity. The selected ratio was deemed sufficient for demonstrating the sensor's analytical performance, which is the primary focus of this study. The two solutions were combined and mixed thoroughly with constant stirring at 700 rpm for 20 minutes, followed by ultrasonication for 10 minutes to ensure proper dispersion. The resulting mixture was transferred into an autoclave and heated at 180 °C for 3 hours. After cooling to room temperature, the product was washed multiple times with ethanol and DI water to remove residual impurities. The final black precipitate of the $NiMn_2O_4$/CNT nanocomposite was dried overnight in a vacuum oven at 70 °C.[37]

### 2.5. Preparation of $NiMn_2O_4$/CNT-GCE electrode

To prepare a clean surface for the GCE prior to modification, the GCE was polished sequentially using alumina slurries with progressively smaller particle sizes of 0.3 μm, 0.1 μm, and 0.05 μm. This gradual polishing process aimed to create a smooth and contaminant-free surface for electrode modification. Following the polishing process, the GCE was thoroughly cleaned by sonicating it repeatedly in ethanol and DI water to remove any residual alumina particles and contaminants. Next, a stable suspension for electrode modification was prepared by dispersing 2 mg of the synthesized $NiMn_2O_4$/CNT nanocomposite in 1 mL of DI water. This suspension was homogenized through vortex mixing and ultrasonication to ensure uniform distribution of the nanocomposite. Subsequently, 8 μL of the $NiMn_2O_4$/CNT suspension was applied onto the cleaned GCE surface and dried using an infrared lamp. The modified electrode, designated as

$NiMn_2O_4$/CNT-GCE, was employed for the electrochemical detection of MTX in this study.

## 3. Results and discussion

### 3.1. Characterization of $NiMn_2O_4$/CNT nanocomposite

The structural and morphological properties of the $NiMn_2O_4$/CNT nanocomposite were comprehensively analyzed using XRD, SEM, TEM, and XPS techniques.

The XRD patterns (Fig. 1A) confirmed the formation of the spinel $NiMn_2O_4$ phase, with diffraction peaks at $2\theta$ values of 17.7°, 29.8°, 35.2°, 36.9°, 43.0°, 53.2°, 56.9°, 62.6°, 74.1°, and 75.1°, corresponding to the (111), (220), (311), (222), (400), (422), (511), (440), (533), and (622) planes, respectively. These peaks match the reference pattern from JCPDS card no. 84-0542 (space group: $R\bar{3}$), verifying the successful synthesis of pure-phase $NiMn_2O_4$. The composite exhibited a broad peak at approximately 21.4°, attributed to the (002) plane of CNTs, confirming their successful integration. The (002) plane of CNTs enhances the composite's electrical conductivity, facilitating efficient electron transfer and providing a stable support network. This integration ensures the structural integrity and functional efficiency of the composite, making it particularly suitable for electrochemical applications.

The chemical composition and oxidation states of the $NiMn_2O_4$/CNT nanocomposite were investigated using XPS (Fig. 1B–F). The survey spectrum (Fig. 1B) revealed the presence of Ni, Mn, O, and C, confirming uniform elemental distribution. High-resolution XPS spectra identified multiple oxidation states for Mn and Ni, which are crucial for redox behavior. The Mn 2p spectrum (Fig. 1C) displayed peaks at 641.7 eV and 644.3 eV for $Mn^{3+}$ and at 653.46 eV and 655.5 eV for $Mn^{4+}$, underscoring their role in enabling efficient redox reactions. Similarly, the Ni 2p spectrum (Fig. 1F) showed peaks at 854.85 eV and 872.4 eV for $Ni^{2+}$, and 856.15 eV and 873.86 eV for $Ni^{3+}$, along with satellite peaks at 861.37 eV and 880.42 eV. The O 1s spectrum (Fig. 1D) revealed three oxygen species: lattice oxygen (530.09 eV), oxygen vacancies (531.5 eV), and adsorbed water molecules (534.01 eV). These oxygen species play a pivotal role in facilitating redox reactions by providing active sites for electron transfer. The C 1s spectrum (Fig. 1E) confirmed successful hybridization with CNTs, showing peaks at 284.8 eV (C–C/C=C), 286.07 eV (C–O), and 289.18 eV (O–C=O).

The surface morphology of the synthesized materials was analyzed using SEM, as shown in Fig. 2. The SEM images of $NiMn_2O_4$ in Fig. 2A and B at different magnifications exhibit rectangular cube-like structures with a porous surface, which can facilitate ion diffusion and improve the electrochemical activity by providing more accessible pathways for electrolyte penetration. This porosity is likely due to $CO_2$ release during the calcination process. In the SEM image (Fig. 2C) of $NiMn_2O_4$/CNT, CNTs are observed coating the rectangular $NiMn_2O_4$ cubes, indicating successful hybridization. Elemental mapping analysis (Fig. 2D–H) confirms the uniform distribution of Ni, C, Mn, and O within the $NiMn_2O_4$/CNT composite. This uniform dispersion ensures structural integrity and facilitates consistent electron transfer pathways, thereby supporting stability and enhancing the electrochemical performance of the electrode material. While nanocubic structures are advantageous for consistent diffusion paths and uniform active sites, the rough surface morphology observed here provides increased surface roughness, potentially enhancing the exposure of active sites and improving electrochemical performance.

To analyze the detailed morphological features of the synthesized materials, TEM analysis was performed. Fig. 3A and B present TEM images of the $NiMn_2O_4$/CNT nanocomposite, showing well-defined nickel manganese oxide-carbon nanotube structures. The images highlight how CNTs are effectively attached to and interacting with the $NiMn_2O_4$ nanoparticles, indicating a strong interaction that enhances conductivity and stability. High-resolution TEM (HRTEM) in Fig. 3C reveals distinct lattice fringes, with

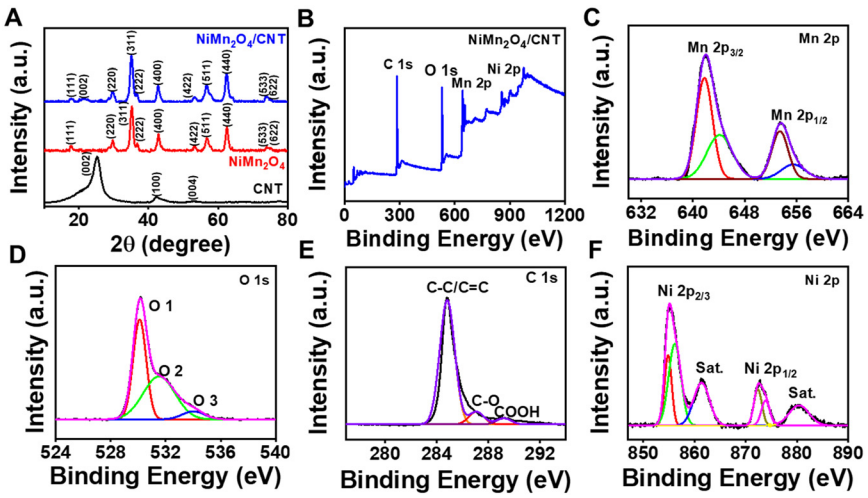


Fig. 1 (A) XRD patterns of CNT, $NiMn_2O_4$, and $NiMn_2O_4$/CNT. (B) XPS survey spectrum of $NiMn_2O_4$/CNT. (C–F) High-resolution XPS spectra of $NiMn_2O_4$/CNT: (C) Mn 2p, (D) O 1s, (E) C 1s, and (F) Ni 2p.

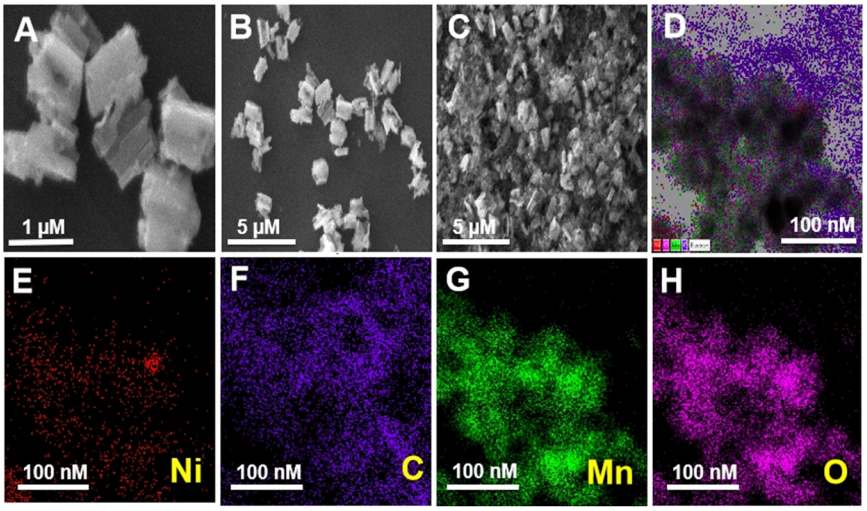


**Fig. 2** SEM images of (A and B) $NiMn_2O_4$ at different magnification (C) $NiMn_2O_4$/CNT. (D–H) Elemental mapping analysis of the $NiMn_2O_4$/CNT nanocomposite showing elements Ni, C, Mn, and O.

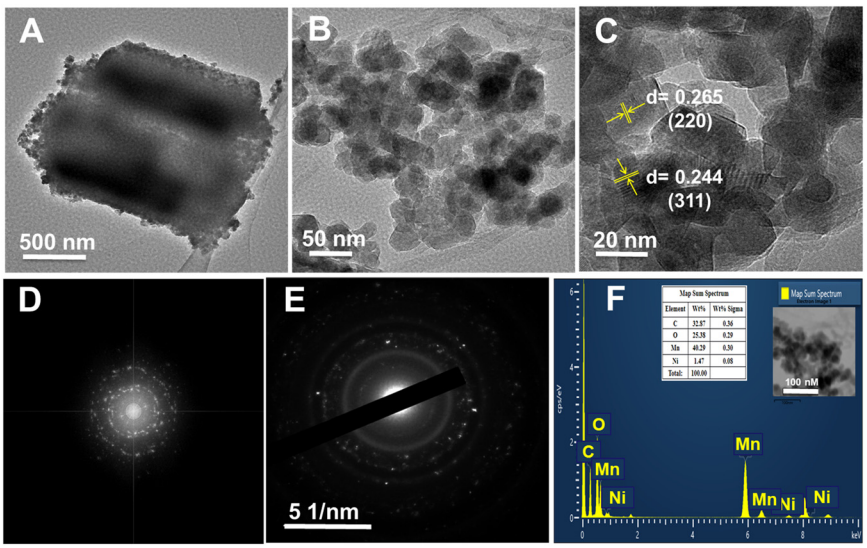


**Fig. 3** (A and B) TEM image of $NiMn_2O_4$/CNT (C) HR-TEM of $NiMn_2O_4$/CNT nanocomposite. (D) FFT pattern of $NiMn_2O_4$/CNT, (E) SAED pattern and (F) EDS analysis of the $NiMn_2O_4$/CNT nanocomposite (inset: corresponding TEM image of the analyzed area and the EDS elemental composition table).

measured interplanar spacings of approximately 0.244 nm and 0.265 nm. These spacings correspond to the (311) and (220) crystal planes of $NiMn_2O_4$, which are critical for facilitating efficient electron transport and enhancing the material's stability during electrochemical processes. The observed crystallinity directly supports the nanocomposite's effectiveness in sensing applications. These spacings are critical as they correspond to the (311) and (220) crystal planes of $NiMn_2O_4$, confirming the material's high degree of crystallinity, which is essential for facilitating efficient electron transport and enhancing electrochemical performance. These spacings correspond to the (311) and (220) crystal planes of $NiMn_2O_4$, consistent with the XRD data at $2\theta$ values of 35.2° and 29.8°, respectively. This confirms the crystallinity of the material. The FFT pattern in Fig. 3D illustrates the crystalline order of the $NiMn_2O_4$/CNT nanocomposite, further supporting the observed lattice fringes. Meanwhile, the selected area electron diffraction (SAED) pattern shown in Fig. 3E demonstrates concentric rings interspersed with bright spots, highlighting the polycrystalline nature of the $NiMn_2O_4$ material. These diffraction rings closely match the XRD peaks, further confirming the integration of $NiMn_2O_4$ nanocubes with CNTs. Additionally, the SAED pattern confirms the presence of the (111), (311), and (400) crystal planes, aligning with the XRD data for $NiMn_2O_4$. This high degree of crystallinity is crucial for enhancing the electrochemical properties of the nanocomposite.

To further confirm the composition, EDS analysis was performed (Fig. 3F). The EDS spectrum reveals distinct peaks

corresponding to Ni, Mn, O, and C, verifying the elemental composition of the $NiMn_2O_4$/CNT nanocomposite. This analysis confirms the successful integration of $NiMn_2O_4$ and CNT components, which is essential for maintaining uniform active sites and ensuring consistent electron transfer pathways. Such uniformity supports structural stability and enhances the nanocomposite's efficiency in electrochemical sensing applications.

### 3.2. Electrochemical behavior of $NiMn_2O_4$/CNT-GCE

The electrochemical performance of the modified electrodes was evaluated using CV and EIS. As shown in Fig. 4A, the $NiMn_2O_4$/CNT-GCE electrode demonstrated the highest anodic peak current ($I_{pa}$ = 39.1 μA) and the lowest peak-to-peak separation ($\Delta E_p$ = 0.105 V) compared to the $NiMn_2O_4$-GCE ($I_{pa}$ = 26 μA, $\Delta E_p$ = 0.120 V), CNT-GCE ($I_{pa}$ = 32 μA, $\Delta E_p$ = 0.110 V), and bare GCE ($I_{pa}$ = 9 μA, $\Delta E_p$ = 0.115 V) electrodes, under conditions of 0.1 M KCl with 5 mM $[Fe(CN)_6]^{3-}$. These findings suggest that the synergistic combination of CNTs and $NiMn_2O_4$ nanoparticles accelerates electron transfer at the $NiMn_2O_4$/CNT-GCE interface, facilitating more efficient redox processes.

EIS measurements were conducted to evaluate the interfacial properties of the electrodes, as shown in Fig. 4B. The Nyquist plots, characterized by a semicircle in the high-frequency region representing charge transfer resistance ($R_{ct}$), revealed distinct differences among the electrodes. The $R_{ct}$ values were determined by fitting the Nyquist plots to a modified Randles equivalent circuit model (Fig. 4B inset), consisting of solution resistance ($R_s$), charge transfer resistance ($R_{ct}$), a constant phase element (CPE), and Warburg impedance (W). Table S1† summarizes the fitted EIS parameters for each electrode. The $NiMn_2O_4$/CNT-GCE exhibited the lowest $R_{ct}$ value (7.98 Ω), indicating significantly enhanced charge transfer kinetics. In contrast, the $NiMn_2O_4$-GCE displayed the highest $R_{ct}$ value (316.75 Ω), attributed to the limited intrinsic conductivity of standalone $NiMn_2O_4$. The bare GCE and CNT-GCE exhibited $R_{ct}$ values of 49.45 Ω and 45.93 Ω, respectively. The slight reduction in $R_{ct}$ for the CNT-GCE reflects the high conductivity of CNTs, which facilitates charge transfer. However, the relatively small improvement suggests that factors such as CNT dispersion and contact resistance on the GCE surface may limit its overall conductivity under the current experimental conditions. The synergy between $NiMn_2O_4$ and CNTs in the composite is critical to the superior performance of the $NiMn_2O_4$/CNT-GCE. While CNTs provide a highly conductive framework for electron transport, the integration of $NiMn_2O_4$ introduces abundant active sites that enhance the electrode's electrocatalytic activity. This balance between conductivity and catalytic efficiency enables the composite to achieve optimal performance, as reflected by its improved CV peak currents and lower $\Delta E_p$ values. These findings underscore the complementary roles of CNTs and $NiMn_2O_4$ in the composite: CNTs contribute to efficient electron transport, while $NiMn_2O_4$ provides catalytic activity and active sites for redox reactions. Together, these components create a highly effective platform for electrochemical sensing applications.

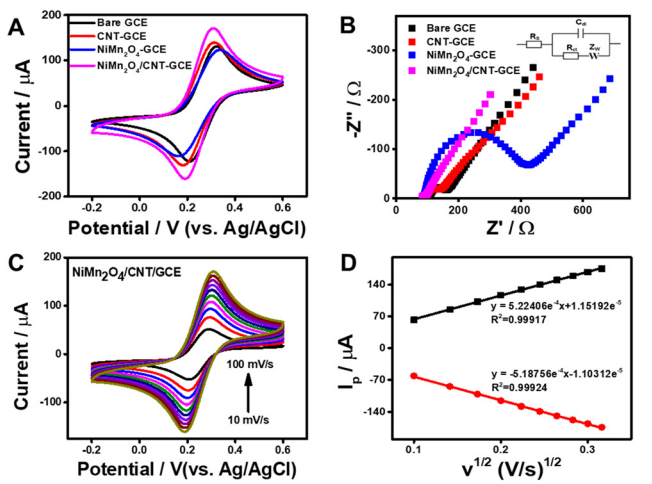


**Fig. 4** (A) CV curves of bare GCE, CNT-GCE, $NiMn_2O_4$-GCE, and $NiMn_2O_4$/CNT-GCE recorded in 5.0 mM $[Fe(CN)_6]^{3-}$ containing 0.1 M KCl at a scan rate of 50 mV $s^{-1}$. (B) Corresponding EIS Nyquist plots for bare GCE, CNT-GCE, $NiMn_2O_4$-GCE, and $NiMn_2O_4$/CNT-GCE. Inset: Randles equivalent circuit model used for fitting EIS data. (C) CV curves of $NiMn_2O_4$/CNT-GCE at varying scan rates (10 to 100 mV $s^{-1}$) in 5.0 mM $[Fe(CN)_6]^{3-}$ containing 0.1 M KCl. (D) Plots of $I_{pa}$ and $I_{pc}$ *versus* $v^{1/2}$, showing linear relationships.

Additionally, the CV analysis performed at different scan rates (10–100 mV $s^{-1}$) (Fig. 4C) showed that the redox peak currents ($I_{pa}/I_{pc}$) increased linearly with the scan rate, confirming that the redox reaction of $[Fe(CN)_6]^{3-}$ at the $NiMn_2O_4$/CNT-GCE interface was controlled by diffusion. This diffusion-controlled process was further validated by the linear relationship between the peak currents ($I_{pa}/I_{pc}$) and the square root of the scan rate ($v^{1/2}$), as shown in Fig. 4D. The electrochemically active surface area (EASA) was calculated using the Randles–Sevcik equation as given below:

$$I_p = (2.69 \times 10^5) n^{3/2} A C D^{1/2} v^{1/2}.$$

In this equation, $I_p$ represents the redox peak currents, $n$ is the number of electrons involved, $v$ is the scan rate (V $s^{-1}$), $A$ denotes the electrochemically active surface area ($cm^2$), $D$ is the diffusion coefficient ($7.6 \times 10^{-6}$ $cm^2$ $s^{-1}$ for $K_3[Fe(CN)_6]$), and $C$ is the concentration of $[Fe(CN)_6]^{3-}$ (5 mmol $L^{-1}$). Based on the slope obtained from Fig. 4D and additional data from Fig. S1† for comparison, the EASA for $NiMn_2O_4$/CNT-GCE was calculated to be 0.098 $cm^2$, which is significantly larger than that of CNT-GCE (0.071 $cm^2$), $NiMn_2O_4$/GCE (0.048 $cm^2$), and bare GCE (0.064 $cm^2$). The larger EASA of $NiMn_2O_4$/CNT-GCE can be attributed to the synergistic effects between $NiMn_2O_4$ nanoparticles and CNTs, which enhance electron transfer and provide a higher density of active sites for electrochemical reactions.[22] Combined with its lower resistance and smaller peak separation observed in Fig. 4A and B, these properties

underscore the remarkable electrochemical sensing potential of $NiMn_2O_4$/CNT-GCE.

In summary, the integration of $NiMn_2O_4$ and CNTs onto the GCE significantly enhances its electron transfer kinetics, increases its current response, and expands its active surface area. These synergistic effects establish $NiMn_2O_4$/CNT-GCE as a promising platform for advanced electrochemical sensing applications.

### 3.3. Electrochemical behavior of $NiMn_2O_4$/CNT-GCE for MTX

Fig. 5A illustrates the CV responses of bare GCE, $NiMn_2O_4$-GCE, CNT-GCE, and $NiMn_2O_4$/CNT-GCE for the detection of MTX (1 μM) in 0.1 M PBS (pH 7) at a scan rate of 100 mV $s^{-1}$. The bare GCE exhibited a low $I_{pa}$ of 22.9 μA at an $E_{pa}$ of 0.877 V, indicating limited electrochemical activity due to its lack of catalytic properties and active sites. $NiMn_2O_4$-GCE demonstrated a slight improvement with an $I_{pa}$ of 27.3 μA and a shift in $E_{pa}$ to 0.846 V, reflecting the catalytic activity and active sites provided by $NiMn_2O_4$. CNT-GCE exhibited a significant enhancement in electrochemical performance, with an $I_{pa}$ of 120.1 μA at an $E_{pa}$ of 0.853 V, attributable to the excellent conductivity, high surface area, and efficient electron transport properties of CNTs. Notably, $NiMn_2O_4$/CNT-GCE showed the highest electrochemical activity, achieving an $I_{pa}$ of 142.6 μA at an $E_{pa}$ of 0.849 V. This remarkable performance highlights the synergistic effect of CNTs and $NiMn_2O_4$, where CNTs facilitate electron transfer through their conductive network and $NiMn_2O_4$ provides abundant active sites for MTX oxidation, resulting in superior sensitivity and electrocatalytic efficiency.

The influence of solution pH on MTX detection was investigated by CV (Fig. 5B and C). As shown in Fig. 5C, the oxidation peak potential ($E_{pa}$) shifted linearly to lower values with increasing pH in the range of 3–7, with a slope of −0.0514 V per pH unit ($R^2$ = 0.996). This value is close to the theoretical Nernstian slope of −0.059 V per pH, indicating that the oxidation process involves a proton-coupled electron transfer (PCET) mechanism, likely consisting of one proton and one electron transfer. At pH values above 7, the $E_{pa}$ plateaued, suggesting diminished proton involvement due to reduced protonation of MTX in alkaline media.

To further support this mechanism, the number of electrons ($n$) involved in the oxidation process was estimated using the Randles–Sevcik equation. The linear dependence of the anodic peak current ($I_{pa}$) on the square root of the scan rate ($\nu^{1/2}$) confirms a diffusion-controlled process. The calculated n value was approximately 1, consistent with a single-electron transfer coupled with a proton, as expected in a PCET process. A schematic illustration of the proposed mechanism is shown in Scheme 2, and detailed calculations are provided in the ESI.† The agreement of our findings with previously reported oxidation mechanisms of MTX[39–41] reinforces the reliability of our proposed pathway. These studies similarly describe a one-electron/one-proton process under comparable pH conditions, supporting the proton-coupled electron transfer mechanism.

Furthermore, the anodic peak current ($I_{pa}$) reached its maximum at pH 7, highlighting the optimal electrochemical response under neutral conditions. At both lower and higher pH values, the $I_{pa}$ decreased, potentially due to reduced electrochemical activity or electrode surface fouling under extreme acidic or basic environments. These findings emphasize the critical role of pH in modulating the electrochemical behavior of MTX at the $NiMn_2O_4$/CNT-GCE interface.

The observed pH-dependent electrochemical behavior can be rationalized by the mechanism illustrated in Scheme 2. Initially, MTX undergoes protonation in the solution phase under acidic conditions. This protonation facilitates a

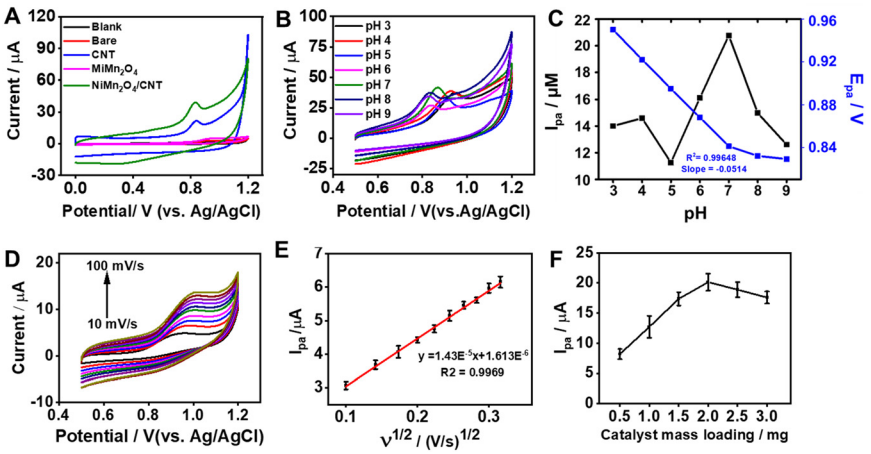


Fig. 5 (A) CV curves of bare GCE, $NiMn_2O_4$-GCE, CNT-GCE, and $NiMn_2O_4$/CNT-GCE recorded in 1 μM MTX at pH 7 with a scan rate of 100 mV $s^{-1}$. (B) CV responses of $NiMn_2O_4$/CNT-GCE in 1 μM MTX under varying pH conditions (pH 3–9). (C) Relationship between pH and $I_{pa}$ (left $y$-axis) and $E_{pa}$ (right $y$-axis), showing a slope of −0.0514 V per pH unit ($R^2$ = 0.99648). (D) CV curves of $NiMn_2O_4$/CNT-GCE at different scan rates (10–100 mV $s^{-1}$) in 1 μM MTX. (E) Plot of $I_{pa}$ *vs.* $\nu^{1/2}$. (F) Optimization of catalyst mass loading on $NiMn_2O_4$/CNT-GCE, showing the impact on $I_{pa}$ in 1 μM MTX.

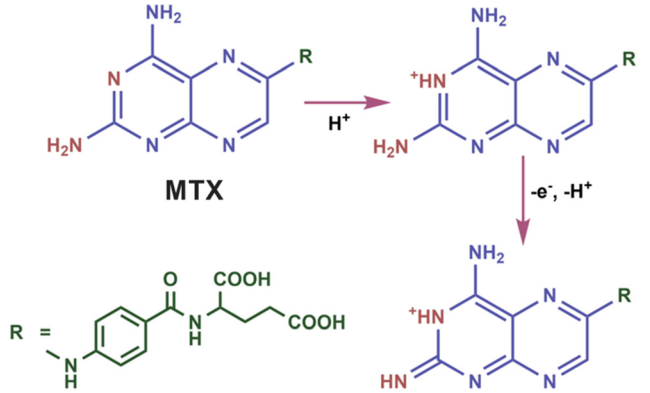


**Scheme 2** Proposed electrochemical oxidation mechanism of MTX at the $NiMn_2O_4$/CNT-GCE interface.

subsequent stepwise process at the electrode surface, where one electron and one proton are transferred ($-1e^-$, $-1H^+$) to form the oxidized species. The linear relationship between $E_{pa}$ and pH up to pH 7 further supports this proton-coupled electron transfer process. Beyond pH 7, the reduced proton availability likely limits the initial protonation step, leading to the observed saturation behavior.

This proposed mechanism aligns well with experimental data, demonstrating the critical role of PCET in the electrochemical oxidation of MTX. The findings provide valuable insights into optimizing the pH conditions for enhanced electrochemical sensing performance.

The CV response of $NiMn_2O_4$/CNT-GCE was recorded at varying scan rates (10–100 mV $s^{-1}$) in 0.1 M PBS containing 1 μM MTX, as shown in Fig. 5D. The $I_{pa}$ increased linearly with the $v^{1/2}$, as presented in Fig. 5E. This linear relationship confirms that the electrochemical reaction is diffusion-controlled, where the redox species near the electrode surface dominate the reaction kinetics. This implies that the availability of MTX molecules at the electrode surface, driven by diffusion, is a critical factor in enabling the PCET mechanism described in Scheme 2. The integration of $NiMn_2O_4$ and CNTs enhances this process by facilitating efficient electron transfer and providing active sites for the PCET reaction.

The influence of catalyst mass loading on the electrochemical response of $NiMn_2O_4$/CNT-GCE was investigated using CV, as illustrated in Fig. 5F. The $I_{pa}$ increased proportionally with catalyst mass loading up to 2 mg, reaching a maximum response. Beyond this point, the $I_{pa}$ began to decrease, likely due to increased diffusion resistance and aggregation of catalyst particles on the electrode surface, which hindered efficient electron transfer. These results confirm that 2 mg is the optimal catalyst loading for achieving the best electrochemical performance. By combining this optimized loading with the diffusion-controlled characteristics established in the previous section, $NiMn_2O_4$/CNT-GCE achieves its peak sensing performance under neutral pH conditions. Based on the experimental findings, the integration of $NiMn_2O_4$ and CNTs in the composite plays a dual role. First, CNTs provide a highly conductive network that enhances electron mobility and reduces charge transfer resistance, as evidenced by the EIS results (Fig. 4B). Second, $NiMn_2O_4$ offers abundant catalytic sites for the PCET mechanism, facilitating efficient redox reactions. Together, these components create a robust platform with the potential for high sensitivity and selectivity in MTX sensing, which will be further validated in subsequent analyses.

### 3.4. Electrochemical sensing performance of $NiMn_2O_4$/CNT-GCE for MTX

The electrochemical sensing performance of the $NiMn_2O_4$/CNT-GCE towards MTX was investigated using DPV in 0.1 M PBS (pH 7.0). Fig. 6A shows the DPV curves obtained at various MTX concentrations ranging from 0.05 to 3.0 μM. A distinct increase in the $I_{pa}$ is observed with increasing MTX concentration, indicating the effective electrocatalytic activity of the $NiMn_2O_4$/CNT nanocomposite towards MTX oxidation.

The relationship between $I_{pa}$ and MTX concentration is illustrated in Fig. 6B. Notably, the calibration curve exhibits two distinct linear ranges. The first linear range spans from 0.05 μM to approximately 0.1 μM, with a linear regression equation of $y = 1.929e^{-6}x - 6.053e^{-6}$ and a correlation coefficient ($R^2$) of 0.991. The second linear range extends from approximately 0.1 μM to 3.0 μM, with a linear regression equation of $y = 2.812e^{-6}x + 1.226e^{-5}$ and an $R^2$ of 0.993. These high $R^2$ values confirm good linearity within both ranges. This bi-linear response can be attributed to changes in the electrochemical behavior of MTX at varying concentration ranges. At lower concentrations (0.05–0.1 μM), the response is likely dominated by efficient electron transfer kinetics and optimal utilization of available active sites on the electrode surface. As the MTX concentration increases (0.1–3.0 μM), surface saturation effects may begin to play a more significant role, potentially influencing the electron transfer rate and contributing to the change in slope observed in the calibration curve. Despite this change in the dominant mechanism, the diffusion-controlled nature of the MTX oxidation, as evidenced by the results in Fig. 5D and E, ensures consistent and reliable sensing performance across the entire detection range.

The limit of detection (LOD) was calculated using the standard formula,

$$LOD = 3\sigma/m$$

where $\sigma$ is the standard deviation of the blank signal, m is the slope of the calibration curve for the lowest concentration range and the LOD, determined using the slope from the first linear range (0.05–0.1 μM), was found to be 0.627 nM.

A comparative analysis (Table 1) highlights the exceptional sensitivity of the $NiMn_2O_4$/CNT-GCE sensor, demonstrating a lower LOD than previously reported electrochemical MTX sensors. Specifically, it surpasses the

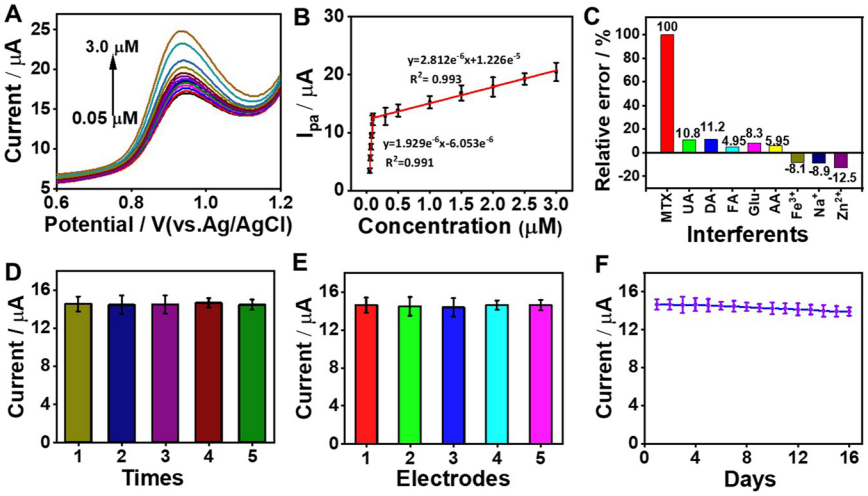


**Fig. 6** (A) DPV curves of $NiMn_2O_4$/CNT-GCE recorded at various MTX concentrations ranging from 0.05 to 3.0 μM in 0.1 M PBS (pH 7.0). (B) Calibration plot showing the relationship between MTX concentration and $I_{pa}$. (C) Relative responses of the $NiMn_2O_4$/CNT-GCE to various interfering species (50 μM each) added to a 1 μM MTX solution in 0.1 M PBS (pH 7.0), normalized to the MTX response (1 μM MTX without any added interferents, set to 100%). (D) Repeatability of the sensor response to 1 μM MTX, evaluated using five consecutive measurements with a single electrode. (E) Reproducibility of the sensor response to 1 μM MTX, evaluated using five independently fabricated electrodes. (F) Long-term stability of the sensor monitored over 16 days with the electrode stored at 4 °C in 0.1 M PBS (pH 7.0).

performance of sensors such as NbO/NbC/rGO/GCE (1.6 nM) and f-CNT/PES (2.9 nM). While some sensors, like $Fe_3O_4$/ppy/Pd/SPGE (0.03–100 μM), exhibit broader linear ranges, the linear range of the $NiMn_2O_4$/CNT-GCE sensor (0.05–3.0 μM) is well-suited for monitoring clinically relevant MTX concentrations, ensuring practical utility for therapeutic drug monitoring. The combination of a low LOD (0.627 nM) and a relevant linear range positions the $NiMn_2O_4$/CNT-GCE sensor as a highly sensitive and practically useful platform for advanced MTX detection.

To evaluate the selectivity of the $NiMn_2O_4$/CNT-GCE sensor, the influence of potential interfering species was investigated using DPV. A solution of 1 μM MTX in 0.1 M PBS (pH 7.0) was used as the base solution. Each interfering species (uric acid (UA), dopamine (DA), folic acid (FA), glucose (Glu), ascorbic acid (AA), $Fe^{3+}$, $Na^+$, and $Zn^{2+}$) was added directly to separate aliquots of this MTX solution to achieve a 50-fold excess concentration (50 μM). The DPV responses of these spiked MTX solutions were then measured as shown in Fig. S2.† Fig. 6C shows the relative responses of the sensor to these species, normalized to the response of the 1 μM MTX solution without any added interferents (set to 100%). Among the tested interferents, $Zn^{2+}$ exhibited the largest relative response (−12.5%), which indicates a minor level of interference with MTX detection. $Zn^{2+}$ was observed to cause the most significant interference in the electrochemical sensing of MTX, resulting in a current reduction of approximately 12.5%. This interference can be attributed to several factors. First, $Zn^{2+}$ may form weak coordination complexes with MTX, leading to subtle shifts in oxidation potential, which could alter the peak current and affect detection accuracy. Additionally, $Zn^{2+}$ may adsorb onto the electrode surface, influencing charge transfer kinetics and further complicating the sensing process. Finally, competition between $Zn^{2+}$ and MTX for active sites on the electrode surface may reduce the effective binding of MTX, leading to a decreased electrochemical response. These combined effects contribute to the observed interference, underscoring the importance of optimizing sensor selectivity to mitigate such influences. The responses to all other tested species were significantly smaller, further indicating negligible interference. Therefore, the $NiMn_2O_4$/CNT-GCE sensor demonstrates good selectivity for MTX detection in the presence of common biological metabolites and inorganic ions.

The repeatability, reproducibility, and stability of the fabricated $NiMn_2O_4$/CNT/GCE sensor are crucial for ensuring its reliability and practical applicability. The repeatability of

**Table 1** A comparative analysis of the linear detection range and LOD for MTX using different methods

| Electrode | Technique | Linear range (μM) | LOD (nM) | Ref. |
|---|---|---|---|---|
| f-CNTPE | SWV | 0.01–1.5 | 2.9 | 33 |
| $Fe_3O_4$/ppy/Pd/SPGE | DPV | 0.03–100 | 7.0 | 42 |
| MCM-41/$Fe_3O_4$/GCE | DPV | 0.01–50 | 3 | 43 |
| 3D-graphene CNT/GCE | DPV | 0.7–100 | 70 | 44 |
| NbO/NbC/rGO/GCE | DPV | 0.1–850 | 1.6 | 45 |
| $NiMn_2O_4$/CNT-GCE | DPV | 0.05–1.0<br>0.1–3.0 | 0.627 | This work |

the sensor was evaluated by performing five consecutive measurements using the same electrode at a fixed MTX concentration of 1 μM in 0.1 M PBS (pH 7.0) (Fig. 6D). The relative standard deviation (RSD) of the peak current for these measurements was calculated to be 0.58%, demonstrating excellent repeatability. Reproducibility was assessed by measuring the response to 1 μM MTX using five independently fabricated $NiMn_2O_4$/CNT/GCEs (Fig. 6E). The RSD of the peak currents obtained from these five electrodes was calculated to be 0.78%, confirming excellent reproducibility of the sensor fabrication method. The long-term stability of the $NiMn_2O_4$/CNT/GCE sensor was investigated by storing the modified electrode at 4 °C in 0.1 M PBS (pH 7.0) and performing measurements daily for 16 days (Fig. 6F). The RSD of the peak current over the 16-day period was calculated to be 1.78%. The sensor retained 94.96% of its initial peak current after 16 days. The slight decrease in current over time may be attributed to gradual degradation of the nanocomposite material or slow leaching of the active material from the electrode surface. These results demonstrate the consistent performance and acceptable long-term stability of the $NiMn_2O_4$/CNT/GCE sensor, highlighting its potential for practical applications in MTX detection.

To evaluate the practical applicability of our proposed sensing method for the detection of MTX in real-world conditions, we conducted tests using spiked human serum and urine samples. The performance of the $NiMn_2O_4$/CNT-GCE sensor was assessed using the standard addition method. Human serum and urine samples were diluted 10-fold in 0.1 M PBS (pH 7.0) to ensure the MTX concentrations fell within the established calibration range. The resulting solutions were thoroughly mixed before analysis. Fig. 7A and C show the DPV responses obtained in spiked serum and urine samples, respectively, at MTX concentrations of 0.2, 0.5, and 1.0 μM. The corresponding calibration plots, illustrating the linear relationship between peak current and MTX concentration, are shown in Fig. 7B and D. The recovery results for both the human serum and urine samples are summarized in Table 2. As shown in Table 2, the recovery rates for MTX in spiked serum samples ranged from 96% to 99%, with RSD values between 2.73% and 5.26% ($n$ = 3). In spiked urine samples, the recovery rates ranged from 97% to 98%, with RSD values between 1.30% and 3.45% ($n$ = 3). These results demonstrate that the newly developed $NiMn_2O_4$/CNT-GCE sensor exhibits adequate recovery rates and acceptable precision for effectively monitoring MTX in complex biological matrices such as serum and urine. The relatively low RSD values indicate good precision and reliability of the proposed method in real sample analysis.

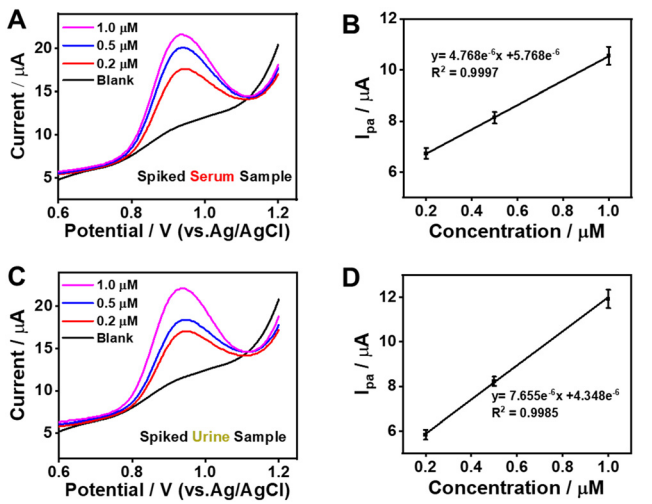


Fig. 7 DPV curves of $NiMn_2O_4$/CNT-GCE obtained for (A) spiked human serum and (C) spiked urine samples with increasing MTX concentrations in 0.1 M PBS (pH 7.0). (B) and (D) show the corresponding linear plots between $I_{pa}$ and MTX concentrations for the serum and urine samples, respectively.

Table 2 Determination of MTX concentrations in real samples using $NiMn_2O_4$/CNT-GCE ($n$ = 3)

| Sample | Spiked (μM) | Found (μM) | Recovery (%) | RSD (%) |
|---|---|---|---|---|
| Serum | 0.2 | 0.198 | 99 | 3.17 |
| | 0.5 | 0.480 | 96 | 2.73 |
| | 1 | 0.980 | 98 | 5.26 |
| Urine | 0.2 | 0.196 | 98 | 2.35 |
| | 0.5 | 0.490 | 98 | 1.30 |
| | 1 | 0.970 | 97 | 3.45 |

## 4. Conclusions

A highly sensitive electrochemical sensor for MTX detection was developed by synthesizing a $NiMn_2O_4$/CNT nanocomposite through a process where $NiMn_2O_4$ nanoparticles, synthesized *via* co-precipitation followed by calcination, were subsequently subjected to hydrothermal treatment in the presence of functionalized multi-walled carbon nanotubes (CNTs). The successful synthesis and synergistic interaction between $NiMn_2O_4$ and CNTs within the nanocomposite were confirmed through XRD, XPS, SEM, and TEM analyses. The resulting $NiMn_2O_4$/CNT-GCE exhibited exceptional electrochemical performance, notably demonstrating an ultralow detection limit of 0.627 nM and a wide linear detection range of 0.05–3.0 μM, significantly surpassing the sensitivity of previously reported MTX electrochemical sensors. This enhanced sensitivity allows for effective monitoring of clinically relevant MTX concentrations. Furthermore, the sensor demonstrated excellent performance in real sample analysis, achieving high recovery rates (96–99%) and low relative standard deviations (RSDs, below 5.26%) in spiked human serum and urine samples, confirming its applicability for accurate and precise MTX detection in complex biological matrices. These combined findings establish the $NiMn_2O_4$/CNT nanocomposite-based sensor as a highly promising platform for clinical diagnostics and therapeutic drug monitoring of

MTX. Future research will focus on further enhancing the sensor's selectivity against a wider range of interferents and evaluating its performance in diverse clinical settings.

## Data availability

The data supporting the findings of this study are available within the article and its ESI.† No additional datasets were generated or analyzed during the current study.

## Conflicts of interest

There are no conflicts to declare.

## Acknowledgements

This work was financially supported by the National Research Foundation of Korea (NRF) grant funded by the Korea Government (MOE and MSIT) (RS-2021-NR060121 and RS-2025-00559158). This research was supported by Korea Basic Science Institute (National research Facilities and Equipment Center) grant funded by the Ministry of Education (RS-2022-NF000922). This research was supported by 'regional innovation mega project' program through the Korea Innovation Foundation funded by Ministry of Science and ICT (2023-DD-UP-0007). This work was also supported by the Soonchunhyang University research fund.

## References

1 M. Krajinovic and A. Moghrabi, *Pharmacogenomics*, 2004, **5**, 819–834.
2 M. Mitsogianni, N. Mitsimponas, S. Haase and A. Giagounidis, *Acta Haematol.*, 2019, **143**, 89–90.
3 D. Levêque, G. Becker, E. Toussaint, L.-M. Fornecker and C. Paillard, *Int. J. Pharmacokinet.*, 2017, **2**, 137–147.
4 B. N. Cronstein and T. M. Aune, *Nat. Rev. Rheumatol.*, 2020, **16**, 145–154.
5 P. Cipriani, P. Ruscitti, F. Carubbi, V. Liakouli and R. Giacomelli, *Expert Rev. Clin. Immunol.*, 2014, **10**, 1519–1530.
6 I. J. Cohen, *J. Neuro-Oncol.*, 2018, **140**, 757.
7 S. C. Howard, J. McCormick, C.-H. Pui, R. K. Buddington and R. D. Harvey, *Oncologist*, 2016, **21**, 1471–1482.
8 R. Jiang, S. Mei and Z. Zhao, *J. Clin. Pharm. Ther.*, 2022, **47**, 1452–1460.
9 M. M. van de Meeberg, H. H. Fidder, B. Oldenburg, J. Sundaresan, E. A. Struys, N. S. M. Montazeri, W. G. N. Mares, N. Mahmmod, D. P. van Asseldonk, M. W. M. D. Lutgens, J. P. Kuyvenhoven, S. T. Rietdijk, L. H. C. Nissen, P. Koehestanie, N. K. H. de Boer, R. de Jonge, G. Bouma and M. Bulatović Ćalasan, the Dutch Initiative on Crohn and Colitis (ICC), *Aliment. Pharmacol. Ther.*, 2023, **58**, 1151–1162.
10 A. Yamuna, N. Karikalan, D. Lee and T. Y. Lee, *J. Hazard. Mater.*, 2023, **451**, 131158.
11 S. Mukherjee, D. Mehta, K. Dhangar and M. Kumar, *Chem. Eng. J.*, 2021, **407**, 127184.
12 M. Markovic, P. A. Neale, B. Nidumolu and A. Kumar, *Ecotoxicol. Environ. Saf.*, 2021, **208**, 111428.
13 Pharmaceutical and Personal Care Products: From Wastewater Treatment into Agro-Food Systems | Environmental Science & Technology, **https://pubs.acs.org/doi/full/10.1021/acs.est.9b06206**, (accessed January 26, 2025).
14 Evaluation of uptake of the cytostatic methotrexate in Elliptio complanata mussels by LC–MS/MS | Environmental Science and Pollution Research, **https://link.springer.com/article/10.1007/s11356-022-19064-7**, (accessed January 26, 2025).
15 S. Santana-Viera, J. Tuček, M. E. Torres-Padrón, Z. Sosa-Ferrera, J. J. Santana-Rodríguez and R. Halko, *Anal. Bioanal. Chem.*, 2020, **412**, 3639–3651.
16 X. Shi, H. Gao, Z. Li, J. Li, Y. Liu, L. Li and Q. Zhang, *BMC Pharmacol. Toxicol.*, 2019, **20**, 3.
17 R. G. Buice, W. E. Evans, J. Karas, C. A. Nicholas, P. Sidhu, A. B. Straughn, M. C. Meyer and W. R. Crom, *Clin. Chem.*, 1980, **26**, 1902–1904.
18 F. Karami, S. Ranjbar, Y. Ghasemi and M. Negahdaripour, *J. Pharm. Anal.*, 2019, **9**, 373–391.
19 R. K. Devi, M. Ganesan, T.-W. Chen, S.-M. Chen, M. Akilarasan, S.-P. Rwei, J. Yu, K.-Y. Lin and A. Shaju, *Process Saf. Environ. Prot.*, 2023, **172**, 986–997.
20 R. Keerthika Devi, M. Ganesan, T.-W. Chen, S.-M. Chen, B.-S. Lou, M. Ajmal Ali, F. M. Al-Hemaid and R.-H. Li, *J. Electroanal. Chem.*, 2022, **923**, 116817.
21 R. Keerthika Devi, M. Ganesan, T.-W. Chen, S.-M. Chen, R. Ahmed Rasheed, W. A. Al-onazi, M. S. Elshikh, X. Liu and J. Yu, *Food Chem.*, 2023, **404**, 134516.
22 N. Abbas, S. J. Jang and T. H. Kim, *Nanomaterials*, 2024, **14**, 775.
23 J. Li, D. Chen, T. Zhang and G. Chen, *Anal. Methods*, 2021, **13**, 117–123.
24 S. Zhang, C. Ye, W. Zhao, L. An, X. Yu, L. Zhang, H. Sun and M. Feng, *Front. Environ. Sci. Eng.*, 2021, **16**, 93.
25 S. Kummari, V. S. Kumar, M. Satyanarayana and K. V. Gobi, *Microchem. J.*, 2019, **148**, 626–633.
26 S. Akhter, Md. Shalauddin, W. J. Basirun, V. S. Lee, S. R. Ahmed, A. R. Rajabzadeh and S. Srinivasan, *Sens. Actuators, B*, 2022, **373**, 132743.
27 S. Tajik, H. Beitollahi, S. Shahsavari and F. G. Nejad, *Chemosphere*, 2022, **291**, 132736.
28 S. J. Rajoba, R. D. Kale, S. B. Kulkarni, V. G. Parale, R. Patil, H. Olin, H.-H. Park, R. P. Dhavale and M. Phadatare, *J. Compos. Sci.*, 2021, **5**, 69.
29 M. Abdullah, S. I. A. Shah, K. Jabbour, P. John, M. F. Ehsan, A. M. Karami, M. N. Ashiq and S. I. Allakhverdiev, *Dalton Trans.*, 2024, **53**, 8680–8691.
30 Q. Qin, L. Chen, T. Wei, Y. Wang and X. Liu, *Catal. Sci. Technol.*, 2019, **9**, 1595–1601.
31 Y. Sun, J. Zhang, X. Sun and N. Huang, *CrystEngComm*, 2020, **22**, 1645–1652.
32 R. Duddi, S. Shivani, A. K. Dhiman, N. Kamboj Singh and S. Kumar, *J. Mater. Sci.: Mater. Electron.*, 2024, **36**, 39.

33 S. Kummari, V. S. Kumar, M. Satyanarayana and K. V. Gobi, *Microchem. J.*, 2019, **148**, 626–633.
34 E. Asadian, S. Shahrokhian, A. Iraji Zad and F. Ghorbani-Bidkorbeh, *Sens. Actuators, B*, 2017, **239**, 617–627.
35 M. S. Cosio, A. Pellicanò, B. Brunetti and C. A. Fuenmayor, *Sens. Actuators, B*, 2017, **246**, 673–679.
36 P. Balasubramanian, T. S. T. Balamurugan, S.-M. Chen and T.-W. Chen, *J. Hazard. Mater.*, 2019, **361**, 123–133.
37 L. Sajjad, G. Ali, M. A. Mansoor and M. F. Khan, *J. Energy Storage*, 2023, **72**, 108351.
38 K. Chandiran and K. C. Nagamuthu Raja, *Colloids Surf., A*, 2023, **667**, 131434.
39 A. Yamuna, N. Karikalan, D. Lee and T. Y. Lee, *J. Hazard. Mater.*, 2023, **451**, 131158.
40 H. R. S. Lima, E. A. de Oliveira Farias, P. R. S. Teixeira, C. Eiras and L. C. C. Nunes, *J. Solid State Electrochem.*, 2019, **23**, 3153–3164.
41 Y. Wei, L. Luo, Y. Ding, X. Si and Y. Ning, *Bioelectrochemistry*, 2014, **98**, 70–75.
42 S. Tajik, H. Beitollahi, S. Shahsavari and F. G. Nejad, *Chemosphere*, 2022, **291**, 132736.
43 M. Ghalkhani and E. Sohouli, *Microporous Mesoporous Mater.*, 2022, **331**, 111658.
44 E. Asadian, S. Shahrokhian, A. Iraji Zad and F. Ghorbani-Bidkorbeh, *Sens. Actuators, B*, 2017, **239**, 617–627.
45 R. Keerthika Devi, M. Ganesan, T.-W. Chen, S.-M. Chen, M. Akilarasan, A. Shaju, S.-P. Rwei, J. Yu and Y.-Y. Yu, *J. Colloid Interface Sci.*, 2023, **643**, 600–612.